Chemistry–A European Journal
Research Article
doi.org/10.1002/chem.202401345
Chemistry Europe
European Chemical Societies Publishing
www.chemeurj.org

Precisely Designed Ultra-Small CoP Nanoparticles-Decorated Hollow Carbon Nanospheres as Highly Efficient Host in Lithium–Sulfur Batteries

Ping Feng,[a] Qingping Wu,[a, b] Yael Rodriguez Ayllon,[a] and Yan Lu*[a, c, d]

Designing porous carbon materials with metal phosphides as host materials holds promise for enhancing the cyclability and durability of lithium–sulfur (Li–S) batteries by mitigating sulfur poisoning and exhibiting high electrocatalytic activity. Nevertheless, it is urgent to precisely control the size of metal phosphides to further optimize the polysulfide conversion reaction kinetics of Li–S batteries. Herein, a subtlety regulation strategy was proposed to obtain ultra-small CoP nanoparticles-decorated hollow carbon nanospheres (CoP@C) by using spherical polyelectrolyte brush (SPB) as the template with stabilizing assistance from polydopamine coating, which also works as carbon source. Leveraging the electrostatic interaction between SPB and Co^{2+}, ultra-small Co particles with sizes measuring 5.5 ± 2.6 nm were endowed after calcination. Subsequently, through a gas-solid phosphating process, these Co particles were converted into CoP nanoparticles with significantly finer sizes (7.1 ± 3.1 nm) compared to state-of-the-art approaches. By uniformly distributing the electrocatalyst nanoparticles on hollow carbon nanospheres, CoP@C facilitated the acceleration of Li-ion diffusion and enhanced the conversion reaction kinetics of polysulfides through adsorption-diffusion synergy. As a result, Li–S batteries utilizing the CoP@C/S cathode demonstrated an initial specific discharge capacity of 850.0 mAh g^{-1} at 1.0 C, with a low-capacity decay rate of 0.03% per cycle.

Introduction

Since their discovery in the 1960s, Lithium–sulfur (Li–S) batteries have become a focal point in advanced energy storage systems, primarily due to their remarkably high theoretical specific capacity (up to 1675 mAh g^{-1}) and cost-effectiveness.[1] Yet, the commercialization of Li–S batteries encounters hurdles such as the low electrical conductivity of sulfur,[2] the slow conversion of lithium polysulfides (LiPSs) intermediates,[3] and the "shuttle effect" caused by LiPSs.[4] To address these challenges, researchers have explored a wide range of strategies, including introducing various carbon materials to confine sulfur,[5] separators modification,[6] or incorporating interlayers.[7] Among those strategies, introducing LiPSs trapper and catalysis centers to facilitate the kinetic conversion between sulfur and lithium sulfide (Li_2S) and to immobilize its intermediate products LiPSs is highly desirable. Considerable attention has been paid to developing catalytic materials with inherent polarity and enhanced conductivity.[8] These materials enable the adsorption and conversion of LiPSs, offering promising solutions to the aforementioned issues. Furthermore, delicate control over the chemical composition (such as elemental doping or defect engineering) of catalytic materials can significantly improve their LiPSs adsorption capability, expedite charge transfer, and facilitate rapid surface reaction kinetics.[1b,9] In this regard, transition metal phosphides (TMPs) have emerged as promising catalysts for enhancing the overall performance of Li–S batteries owing to their notable electrocatalytic activity, stability, and resilience against sulfur poisoning. TMPs are recognized as quasi-platinum catalysts because of their plentiful coordinate unsaturated surface atoms, robust electrical and chemical stability, and exceptional mechanical strength.[1a] Qian and co-workers recently demonstrated that among four cobalt-based compounds (CoP, Co_4N, CoS_2, and Co_3O_4), CoP exhibits the highest rate capability for Li–S batteries. This superiority is attributed to its moderate adsorption capability and excellent diffusion dynamics.[10]

Maximizing the utilization of catalytic materials in Li–S batteries is crucial, necessitating the full exposure of catalytic active sites due to their zero-capacity contribution.[1b,11] Recently, transition metal phosphide quantum dots with size around 3 nm, characterized by an ultrahigh specific surface area, have shown effectiveness in accelerating conversion kinetics due to their unique catalytic properties and maximized

[a] P. Feng, Q. Wu, Y. Rodriguez Ayllon, Y. Lu
Institute of Electrochemical Energy Storage, Helmholtz-Zentrum Berlin für Materialien und Energie, Berlin 14109, Germany
E-mail: yan.lu@helmholtz-berlin.de
[b] Q. Wu
Chongqing Institute of Green and Intelligent Technology, Chinese Academy of Sciences, Chongqing 400714, China
[c] Y. Lu
Institute for Technical and Environmental Chemistry, Friedrich-Schiller-Universität Jena, Jena 07743, Germany
[d] Y. Lu
Helmholtz Institute for Polymers in Energy Applications Jena (HIPOLE Jena), Jena 07743, Germany

Supporting information for this article is available on the WWW under https://doi.org/10.1002/chem.202401345

atom efficiency.[12] However, challenges such as agglomeration induced by high surface energy, ambiguous local atomic environments, and demanding advanced synthesis methods hinder the feasibility of transition metal phosphide quantum dots in commercial LSBs.[1b,4c,13] Meanwhile, TMPs synthesized via metal-organic framework or hydrothermal methods followed by high-temperature calcination have been extensively reported, yet they suffer from TMPs aggregation during calcination, resulting in oversized particles (30–500 nm) with uneven distribution and low catalytic activity.[14] Therefore, achieving sustainability and simplicity in synthesis with controlled particle size is crucial for the development of TMPs-based efficient host materials for Li–S batteries. The gas-solid reaction preparation process offers simplicity in operation without requiring harsh conditions such as high temperature and pressure, making it the most promising method for metal phosphide preparation.[14b]

In this work, ultra-small CoP nanoparticles-decorated hollow carbon nanospheres (CoP@C) were meticulously designed via two steps. Firstly, hollow carbon nanospheres embedded with ultra-small Co nanoparticles were prepared by using the spherical polyelectrolyte brush (SPB) as the template and assisted by polydopamine (PDA) coating, which works as the carbon source. Uniform Co nanoparticles (5.5 ± 2.6 nm) embedded in hollow carbon nanospheres were achieved after calcination in inert gas, benefited from the electrostatic interaction between negatively charged brushes in SPB and Co^{2+} from the cobalt precursor. Secondly, Co nanoparticles were converted to CoP (7.1 ± 3.1 nm) by a gas-solid phosphating process utilizing $NaH_2PO_2 \cdot H_2O$ as the phosphorus source. CoP@C can facilitate the conversion reaction of LiPSs, suppress the LiPSs shuttle, and enhance the cycling stability of the Li–S batteries. Additionally, hollow carbon nanospheres provided enough space for sulfur loading, facilitating rapid electron transfer within the electrode and enhancing sulfur utilization. Consequently, Li–S coin cells constructed with CoP@C/S electrode delivered a high initial discharge capacity of 850.0 mAh g^{-1} at 1.0 C, which was kept at 612.0 mAh g^{-1} after 900 cycles.

Results and Discussion

SPB templates with uniform shape and size (the hydrodynamic diameter of the PS core is 100.0 ± 28.6 nm and the SPB is 340.5 ± 114.1 nm according to Dynamic Light Scattering (DLS) measurements, respectively, as plotted in Figure S1) were first synthesized according to our previous report.[15] Transmission electron microscopy (TEM) image exhibits homogeneous spherical particles with a diameter of ca.100 nm, as shown in Figure S2. The TEM image does not indicate any brushes on the surface of polystyrene due to the "dry effect" during TEM sample preparation.[15b] SPB with long chains of poly(styrene sulfonate) as the brush layer (Figure 1) has rich negative charges. Due to the counter ion exchange of the SPB particles with the positively charged inorganic precursors, it can serve as an efficient template for the synthesis of various hybrid particles.[3c] Figure 1 shows the synthesis route of CoP@C nanospheres using SPB as the template. Firstly, cobalt-nitrate hexahydrate ($Co(NO_3)_2 \cdot 6H_2O$) was dissolved in the aqueous SPB solution. After an ion exchange process between Co^{2+} and the counter-ion of SPB (Na^+), Co^{2+} ions were restricted in the brush layer by the electrostatic interaction (the sample is termed as SPB@Co^{2+}). The electrostatic interaction between Co^{2+} and SPB was confirmed by the decreased hydrodynamic diameter of SPB solution with $Co(NO_3)_2 \cdot 6H_2O$ in the DLS measurement (Figure S1). Following this, a polydopamine (PDA) layer was coated onto the surface of SPB@Co^{2+} (referred to as SPB@Co^{2+}@PDA) to preserve its spherical structure throughout the subsequent calcination process. The TEM image (Figure 2a) confirms the well-preserved spherical shape of the SPB@Co^{2+}@PDA particles after PDA coating, with the PDA layer thickness measured at approximately 15 nm. After calcination, Co nanoparticles embedded in hollow carbon nanospheres (termed as Co@C) were obtained. TEM images of the Co@C nanospheres (Figures 2b, c) reveal that ultra-small Co nanoparticles (5.5 ± 2.6 nm, Figure S3a) are embedded in the hollow carbon nanospheres measuring 90 nm in diameter and 12 nm in thickness. In comparison, Co@C nanospheres synthesized by using pure polystyrene nanospheres as the template resulted in aggre-

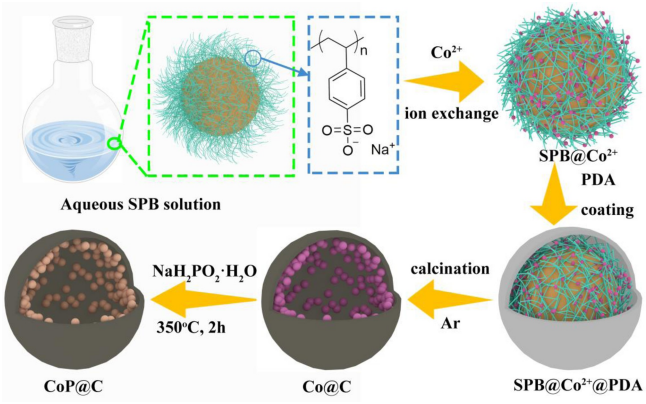

Figure 1. Schematic illustration of the synthesis route to CoP@C nanospheres.

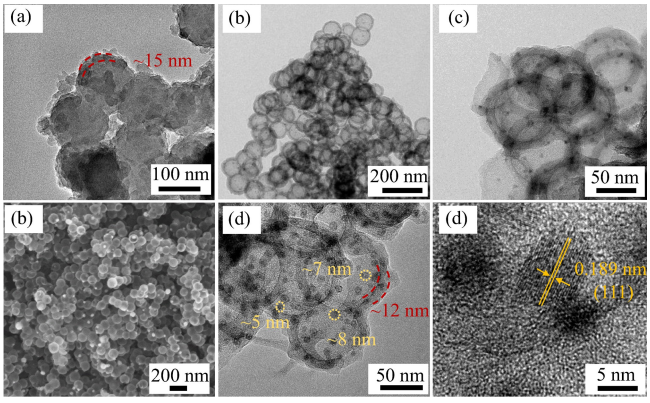

Figure 2. (a) TEM image of the SPB@Co^{2+}@PDA nanospheres. (b, c) TEM images of the Co@C nanospheres. (d) SEM, (e) TEM, and (f) HRTEM images of the CoP@C nanospheres.

gated Co nanoparticles with a size of 30–50 nm, as seen in Figure S4. This result demonstrates the crucial role of the brush layer in the synthesis of ultra-small Co nanoparticles.

Co@C nanospheres were further phosphorized into CoP@C in a gas-solid reaction by using $NaH_2PO_2 \cdot H_2O$ as the phosphorus source.[14a,16] Scanning electron microscopy (SEM) and TEM images of the CoP@C nanospheres (Figures 2d, e) indicate that the particles maintain the initial hollow spherical morphology with CoP nanoparticles with a size of 7.1 ± 3.1 nm (Figure S3b) homogeneously embedded into the hollow carbon nanospheres. High-resolution TEM (HRTEM) image of the CoP@C nanospheres reveals adjacent lattice spacing of 0.189 nm, as shown in Figure 2f, corresponding to the (111) plane of CoP. The specific surface area of the CoP@C is 170.8 $m^2 g^{-1}$, with most pores distributed around 5.5 nm, as shown in Nitrogen adsorption – desorption isotherms in Figure S5. Thermogravimetric Analysis (TGA) indicates the CoP content inside the CoP@C nanospheres is 23.6 wt %, calculated based on the Co_3O_4 residual as shown in Figure S6. In addition, hollow carbon nanospheres (HC) were synthesized as the reference sample using the same method without the addition of $Co(NO_3)_2 \cdot 6H_2O$. The TEM image of HC, as shown in Figure S7, shows a hollow spherical shape with a diameter of 90 nm and thickness of 12 nm, similar to that of the CoP@C nanospheres.

X-ray diffraction (XRD) and X-ray photoelectron spectroscopy (XPS) were employed to examine the crystalline structure and chemical composition of the CoP@C particles. As shown in Figure 3a, the XRD pattern of the HC particles reveals the absence of peaks, suggesting their amorphous nature. Following the introduction of $Co(NO_3)_2 \cdot 6H_2O$ into the SPB solution, the XRD pattern of the Co@C particles exhibits three distinct peaks located at 2θ of 46.4°, 53.6°, and 78.2°, corresponding to the metallic Co (JCPDS No. 88-2325). After gas-solid phosphating of Co@C particles, all peaks in the XRD pattern of the CoP@C particles can be attributed to CoP (JCPDS No. 29–0497), indicating the successful conversion of metallic Co to CoP without the presence of any impurities. XPS spectra offer additional insights into the surface composition and chemical states of the CoP@C nanospheres, as depicted in Figures 3b–d. The high-resolution Co 2p spectrum (Figure 3b) reveals main peaks at 777.1 eV, 780.9 eV, and a satellite peak at 785.3 eV in the Co 2p3/2 region, along with main peaks at 792.3 eV, 797.2 eV, and a satellite peak at 802.3 eV in the Co 2p1/2 region.[16] In the P 2p region (Figure 3c), there is a broad peak at 132.6 eV, indicating the P–O bond, accompanied by two smaller peaks at 127.9 and 129.1 eV, attributed to the metallic Co–P bond. The notable intensity of the P–O peak suggests the susceptibility of CoP to oxidation in the air.[17] In the high-resolution C 1s spectrum (Figure 3d), three primary peaks were detected at 284.6 eV, 285.5 eV, and 287.5 eV, corresponding to the C–C/C=C, C–N, and C=O bonds, respectively.[18] The results from XRD and XPS analyses validate the successful synthesis of CoP@C nanospheres.

To investigate the adsorption ability of CoP@C, Co@C, and HC nanospheres toward LiPSs, a static adsorption experiment was conducted using a 2 mM Li_2S_8 solution in 1,3-dioxolane (DOL)/1,2-dimethoxyethane (DME) solution (V_{DOL}: V_{DME} = 1:1) as a representative polysulfide, as illustrated in Figure 4a.[19] The Li_2S_8 solution was prepared by the chemical reaction between S and Li_2S in the Ar-filled glove box. Subsequently, 20 mg of CoP@C, Co@C, and HC nanoparticles were introduced into 4 mL of the prepared Li_2S_8 solution and individually sealed in glass bottles, respectively. After allowing the mixture to stand for 1 hour, a noticeable decrease in the color intensity of the Li_2S_8 solution was observed, indicating the adsorption of LiPSs by the host materials. Particularly, the Li_2S_8 solution mixed with CoP@C appeared nearly colorless, suggesting the superior polysulfide adsorption capability of the CoP@C nanoparticles compared to

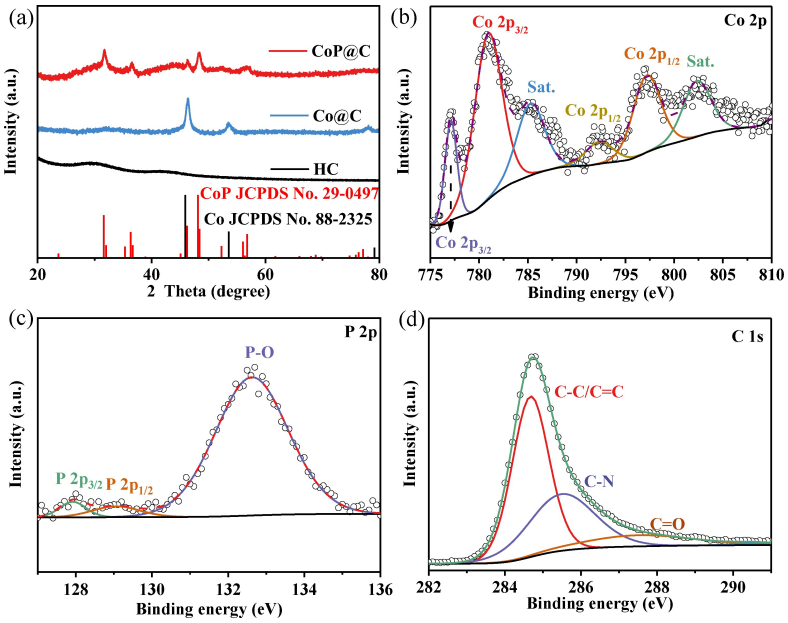

Figure 3. (a) XRD pattern of the CoP@C, Co@C, and HC nanospheres. XPS spectra of the (b) Co 2p, (c) P 2p, and (d) C 1s of the CoP@C nanospheres.

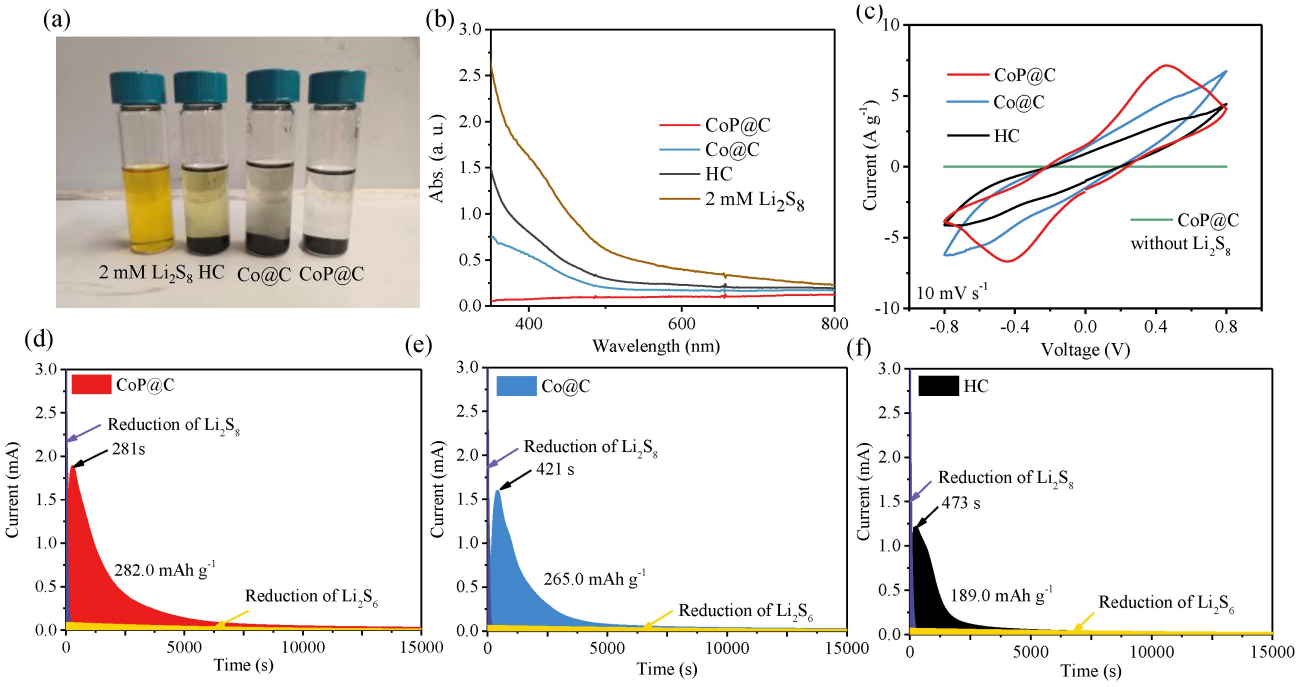

Figure 4. (a) Photographs of the Li_2S_8 solutions (4 mL, 2 mM, dissolved in DME/DOL) after mixing with 20 mg of CoP@C, Co@C, and HC nanoparticles for 1 h. (b) UV-vis absorption spectra of the Li_2S_8 electrolyte after mixing with CoP@C, Co@C, and HC for 1 h. (c) Cyclic voltammetry of the Li_2S_8 symmetric cell with CoP@C, Co@C, and HC nanoparticles as electrodes with a scan rate of 10 mV s^{-1} in a voltage range of −0.8 V to 0.8 V. Fitting of the current-time curves for constant voltage discharge at 2.05 V on (d) CoP@C, (e) Co@C, and (f) HC-based electrodes.

the Co@C and HC nanoparticles. The supernatant Li_2S_8 solutions treated with different host materials were then subjected to Ultraviolet-visible (UV-vis) spectroscopy, as depicted in Figure 4b. UV-vis analysis showed that the Li_2S_8 solution treated with CoP@C nanoparticles showed the minimal absorption within the wavelength range of 350–600 nm, validating its superior polysulfide adsorption capability. To measure the adsorption kinetics for the CoP@C, Co@C, and HC nanoparticles, UV-vis spectroscopy of the Li_2S_8 solution was measured at the initial, after 15 min, 30 min, and 1 h of adsorption with CoP@C, Co@C, and HC, respectively. The absorption intensity at 410 nm at different adsorption times for these three samples was plotted in Figure S8. The fastest Li_2S_8 adsorption kinetics of CoP@C compared to that of Co@C and HC further proves its excellent polysulfide adsorption ability. This finding aligns with previous Density-functional theory calculations, which demonstrated that CoP exhibits stronger adsorption capabilities compared to Co for LiPSs species.[20] This adsorption effectiveness is crucial for mitigating the LiPSs shuttle, thereby improving the cycling performance of Li–S batteries.

Cyclic voltammetry (CV) was employed to investigate the catalytic effect of CoP@C, Co@C, and HC nanoparticles on the redox reaction of LiPSs using Li_2S_8 symmetrical cells. Figure 4c illustrates the current response of the Li_2S_8 symmetrical cell utilizing various host materials across the voltage window of −0.8 V to 0.8 V, with a scan rate of 10 mV s^{-1}. The area under the CV curves represents the capacity of the Li_2S_8 symmetrical cells. Symmetrical cells without Li_2S_8 solution exhibited no capacity, indicating that double-layer capacitance did not contribute to the overall current. The Li_2S_8 symmetrical cells with HC electrode displayed a weak current response due to the limited catalytic effect of HC on the redox reaction of LiPSs. However, upon introducing Co and CoP into the HC nanospheres, the current response significantly increased, indicating that the Co and CoP can efficiently facilitate the electrochemical reactions of LiPSs. Notably, Li_2S_8 symmetrical cells employing the CoP@C electrode exhibited the highest current density and narrowest polarization overpotential, suggesting significant enhancement in LiPSs conversion reactions upon the incorporation of CoP nanoparticles into hollow carbon nanospheres.

For a deeper investigation into the catalytic effects of different host materials on nucleation and growth of solid Li_2S, a Li_2S precipitation experiment was conducted, as previously reported (see Experimental section[21]). Figure 4(d–f) depicts the discharge curves of CoP@C, Co@C, and HC electrodes, respectively, kept at a fixed voltage of 2.05 V for a duration of 15,000 seconds. The area beneath the current curves was analyzed employing two exponential functions, which correspond to the reduction of Li_2S_8 and Li_2S_6, alongside a residual peak indicating the precipitation of Li_2S. Remarkably, the CoP@C electrode exhibited the highest Li_2S precipitation capacity at 282.0 mAh g^{-1}, signifying its superior catalytic effect in Li_2S precipitation compared to that of Co@C (265.0 mAh g^{-1}) and HC electrodes (189.0 mAh g^{-1}). Additionally, the current peak of the CoP@C electrode appeared around 281 s, earlier than that of the Co@C electrode at approximately 421 s and the HC electrode at approximately 473 s. This result suggests the efficient role of CoP@C in promoting the conversion reaction

from Li_2S_4 to Li_2S by incorporating ultra-small CoP nanoparticles into carbon nanospheres.

To further substantiate the positive effect of the CoP@C electrode on promoting the redox reaction process of LiPSs, the lithium-ion diffusion coefficient was determined by CV measurements at different scan rates.[22] The composite sulfur cathode was prepared according to previous report[23] and the samples were termed as CoP@C/S, Co@C/S, and HC/S, respectively. Thermogravimetric Analysis (TGA) reveals that the S content inside the CoP@C/S is 81.7 wt %, as depicted in Figure S9. Figure S10 illustrates the CV curves of the CoP@C/S, Co@C/S, and HC/S electrodes, scanned at 0.1 mV s^{-1} within a voltage range of 1.7 V to 2.8 V. Both CV curves exhibit two cathodic peaks and two anodic peaks: the first cathodic peak (peak C1) at 2.3 V corresponds to sulfur reduction into long-chain LiPSs, while the second cathodic peak (peak C2) at 2.0 V corresponds to further reduction into short-chain LiPSs. The first anodic peak (peak A1) at 2.3 V corresponds to short-chain LiPSs oxidation into long-chain LiPSs, and the second anodic peak (peak A2) at 2.4 V corresponds to further oxidation into elemental sulfur. The CoP@C/S electrode demonstrates the highest current density, attributed to its superior catalytic effect on LiPSs' redox reaction, compared to Co@C/S and HC/S electrodes.

CV measurements of CoP@C/S, Co@C/S, and HC/S electrodes were conducted at varying scan rates from 0.1 to 1.0 mV s^{-1}, within a voltage window of 1.7–2.8 V (*vs.* Li/Li^+). All electrodes displayed two cathodic peaks and two merged anodic peaks (Figure 5a–c) across all scan rates. Despite increased current response with higher scan rates, the shape of the redox peaks remained consistent, indicative of good electrochemical stability. The CV curves of the CoP@C/S, Co@C/S, and HC/S electrodes with a scan rate of 1.0 mV s^{-1} in a voltage range of 1.7 V to 2.8 V were compared, as shown in Figure S11. The first cathodic peak positions on the CV curves were observed at 2.32 V, 2.24 V, and 2.27 V for the CoP@C/S, Co@C/S, and HC/S electrodes, respectively, and their second cathodic peaks were located at 1.95 V, 1.91 V, and 1.93 V for the CoP@C/S, Co@C/S, and HC/S electrodes, respectively. The earlier occurrence of the cathodic peak in the CoP@C/S electrodes indicates the catalytic efficacy of CoP@C in facilitating the conversion reactions of LiPSs. Cathodic and anodic peaks (peak C1, peak C2, peak A1, and peak A2) of all electrodes exhibited a linear relationship with the square root of scanning rates (Figures 5d–f and S12), suggesting a diffusion-limited process.[22a] Consequently, the Li^+ diffusion coefficient can be estimated using the Randles-Sevick equation (1):

$$I_{p=}(2.69 \times 10^5)\, n^{1.5}\, A D_{Li}^{0.5}\, C_{Li}\, v^{0.5} \quad (1)$$

Here, I_p, n, A, D_{Li}, C_{Li}, and v represent the peak current, the number of electrons transferred, the surface area of the electrode, the Li^+ diffusion coefficient, the concentration of lithium ions in the cathodes, and the scan rate, respectively. In this case, n, A, and C_{Li} can be regarded as constant. Therefore, the slope of the curve ($I_p/v^{0.5}$) represents the Li^+ diffusion coefficient. The fitted line and corresponding slope for peak C1, peak C2, peak A1, and peak A2 are depicted in Figures 5d–f and S12, respectively. During the cathodic scan, the CoP@C/S electrode exhibited higher Li^+ diffusivity than HC in peak C2 but lower in peak C1, suggesting that the polar CoP nanoparticles favored the conversion of LiPSs to Li_2S_2/Li_2S rather

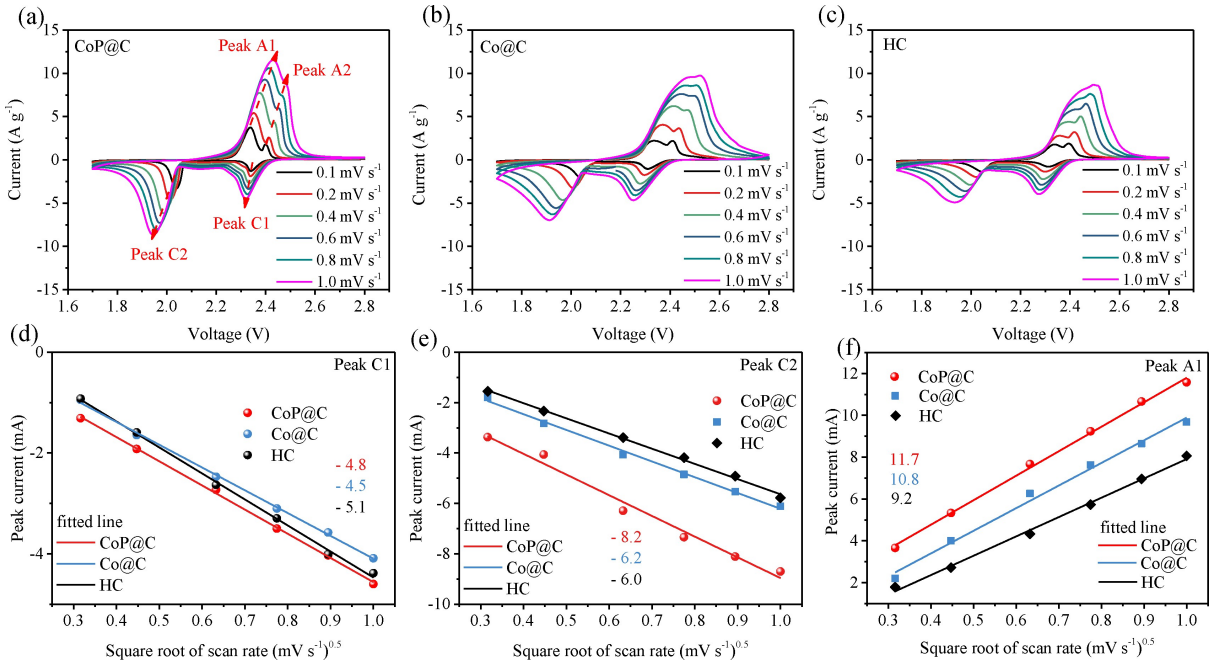

Figure 5. Cyclic voltammetry of the coin cell with the (a) CoP@C/S, (b) Co@C/S, and (c) HC/S electrodes in the voltage range of 1.7–2.8 V at various scan rates of 0.1, 0.2, 0.4, 0.6, 0.8, and 1.0 mV s^{-1}. The plot of CV peak current of (d) the cathodic reaction 1 (peak C1, $S_8 \rightarrow Li_2S_4$), (e) the cathodic reaction 2 (peak C2, $Li_2S_4 \rightarrow Li_2S$), and (f) the anodic reaction 1 (peak A1, $Li_2S \rightarrow Li_2S_4$) versus the square root of scan rate.

than S to LiPSs due to the strong adsorption of long-chain LiPSs by CoP compared to that of short-chain LiPSs and the rapid conversion of the short-chain polysulfides.[24] Conversely, during the anodic scan, the CoP@C/S electrode displayed higher lithium-ion diffusivity than HC in both peaks A1 and A2, indicating the efficient catalysis of the oxidation reaction of Li_2S to S by CoP@C nanoparticles.

To highlight the benefits of CoP@C nanospheres as host materials for Li–S batteries, the electrochemical performance of CoP@C/S, Co@C/S, and HC/S electrodes was evaluated in 2032-coin cell. Figure 6a illustrates the specific discharge capacity of Li–S batteries based on these electrodes at a current density of 0.1 C (1 C = 1,675 mA g^{-1}), with sulfur loading of 1.5 mg cm^{-2} and electrolyte to sulfur ratio (E/S) of 15 μL mg^{-1}. The CoP@C/S electrode exhibited an initial specific discharge capacity of 1,234.6 mAh g^{-1}, alongside an initial coulombic efficiency of 98.7%, notably higher than that of Co@C/S (1,090.5 mAh g^{-1}) and HC/S electrodes (1,069.1 mAh g^{-1}). After 80 cycles, the CoP@C/S electrode maintained a specific discharge capacity of 1,075.6 mAh g^{-1} with a high coulombic efficiency of 97.7%, resulting in a capacity retention rate of 87.1%. In contrast, the Co@C/S and HC/S electrodes only retained specific discharge capacities of 943.1 and 513.1 mAh g^{-1} after 80 cycles at 0.1 C, corresponding to capacity retention rates of 86.5% and 48.0%, respectively. The galvanostatic charge-discharge (GCD) curves of CoP@C/S, Co@C/S, and HC/S electrodes are depicted in Figure 6b, showing two discharge plateaus located at 2.3 V and 2.1 V, and two charge plateaus located at 2.3 V and 2.4 V, consistent with the CV results. The specific discharge capacity of the CoP@C electrode without sulfur was measured at the same condition and the results are presented in Figure S13. The zero capacity of the CoP@C electrode indicates that all capacities of the CoP@C/S electrode are coming from sulfur. The polarization of the three cathode materials was supplemented in Figure S14. The overpotential (ΔV) between the charge and discharge curve was calculated to be 0.20 V, 0.22 V, and 0.23 V for CoP@C/S, Co@C/S, and HC/S cathode, respectively. The slightly lower overpotential of the CoP@C/S cathode compared to that of Co@C/S and HC/S electrodes further proves the good catalytic activity of the CoP@C nanosphere for the redox reaction of sulfur.

To further prove the catalytic activity of the CoP@C/S, Co@C/S, and HC/S electrodes toward the LiPS conversion reaction, Q2/Q1 was calculated, which serves as a reliable indicator for evaluating sulfur interfacial kinetics.[1a,25] Q1 and Q2 denote the capacity of the two discharge plateaus (Figure 6b), as classified in the following two stages:

$$\text{Stage 1}: \quad xS_8 + 16e^- + 16Li^+ \leftrightarrow 8Li_2S_x \quad (4 \le x \le 8) \tag{2}$$

$$\text{Stage 2}: \quad 4Li_2S_x + (6x-8)e^- + (6x-8)Li^+ \leftrightarrow xLi_2S_2 + 2xLi_2S \tag{3}$$

In Stage 1, sulfur reduction to soluble Li_2S_x occurs, representing 1/4 of the theoretical capacity of sulfur. Stage 2, beginning from the lower plateau, involves the reduction of soluble Li_2S_x to Li_2S_2/Li_2S, constituting 3/4 of the total sulfur capacity. The value of Q2/Q1 was calculated to be 1.92 for the CoP@C/S electrode, which is higher than that of the Co@C/S electrode (1.86) and HC/S electrode (1.45) due to the high catalytic effect of CoP nanoparticles.

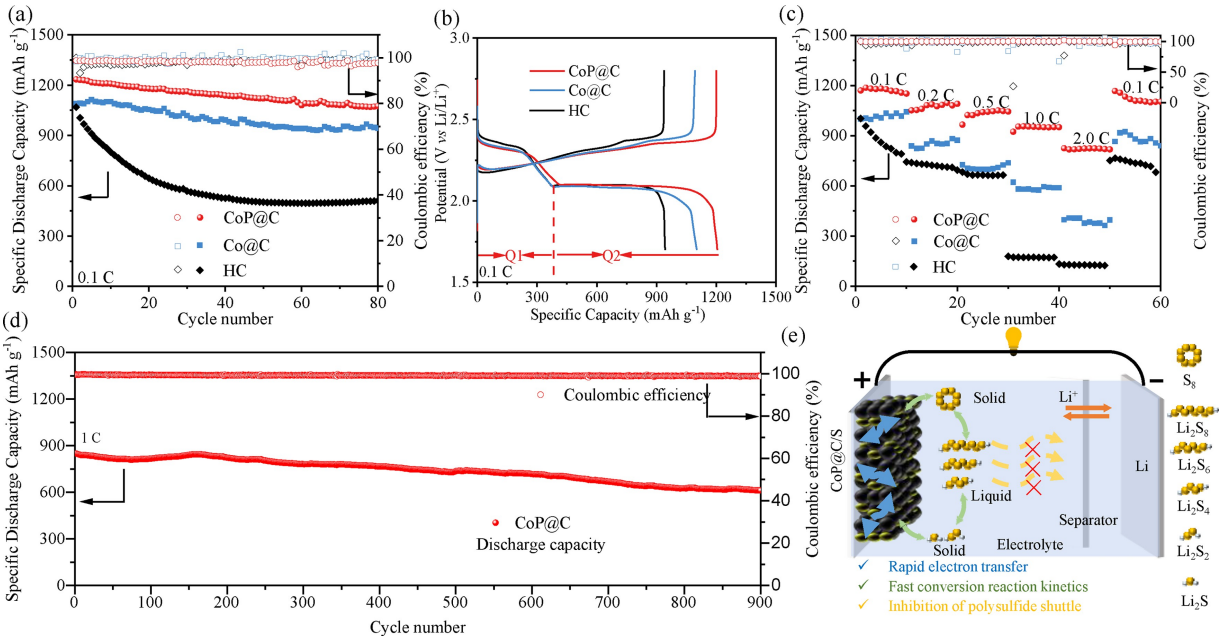

Figure 6. (a) Specific discharge capacity of the Li–S batteries based on CoP@C/S, Co@C/S, and HC/S electrodes at 0.1 C for 80 cycles. (b) GCD curves of the Li–S batteries based on CoP@C/S, Co@C/S, and HC/S electrodes at 0.1 C. (c) Rate performance of the Li–S batteries based on CoP@C/S, Co@C/S, and HC/S electrodes. (d) The specific discharge capacity of the Li–S batteries based on CoP@C/S electrode under a current density of 1.0 C for 900 cycles. (e) Schematic illustration of the advantages of the CoP@C/S electrode in Li–S batteries.

Figure 6c illustrates the rate performance of CoP@C/S, Co@C/S, and HC/S electrodes at various current densities ranging from 0.1 C to 2.0 C. The specific discharge capacities of the CoP@C/S electrode decreased from 1,186.7 to 1,088.4, 1,040.9, 952.9, and 821.6 mAh g^{-1} as the current densities increased from 0.1 to 0.2, 0.5, 1.0, and 2.0 C, respectively. Notably, when the current density was reverted to 0.1 C, the specific discharge capacity was maintained at 1,111.9 mAh g^{-1}, demonstrating the excellent rate capacity of the CoP@C/S cathode. In contrast, the specific discharge capacities of the Co@C/S and HC/S electrodes at 0.1, 0.2, 0.5, 1.0, and 2.0 C were 901.9, 869.5, 698.3, 576.2, 378.4 mAh g^{-1} and 885.0, 727.4, 663.9, 172.0, 126.2 mAh g^{-1}, respectively, all lower than that of the CoP@C/S electrode. GCD curves of the CoP@C/S, Co@C/S, and HC/S electrodes at different current densities are depicted in Figures S15-17, respectively. Electrochemical impedance spectroscopy (EIS) of the CoP@C/S, Co@C/S, and HC/S electrodes before cycling is shown in Figure S18. EIS shows a semicircle in the high-frequency region denoting the charge-transfer process at the interface, while a linear section in the low-frequency region represents lithium diffusion within the electrode.[18] According to the fitting results in Table S1 (Supporting Information), the charge transfer resistance (R_{ct}) of the CoP@C/S electrode was only 44.5 Ω, lower than that of Co@C/S (47.0 Ω) and HC electrodes (54.0 Ω), likely due to the ultra-small size of CoP and its metalloid properties. The smaller R_{ct} of the CoP@C/S electrode indicates faster electronic mobility and improved electrochemical kinetics compared to Co@C/S and HC electrodes. Additionally, the extended cycling performance of the CoP@C/S electrode was assessed at a current density of 1.0 C with sulfur loading of 1.5 mg cm^{-2} and an E/S ratio of 15 μL mg^{-1}, as depicted in Figures 6d and S14. The initial specific discharge capacity reached 850.0 mAh g^{-1} and remained stable at 612.0 mAh g^{-1} after 900 cycles, exhibiting high coulombic efficiency (99.2%) and minimal capacity decay (0.03% per cycle). The electrochemical performance of the CoP@C/S electrode at 1.0 C was compared to other recently reported metal phosphides, as summarized in Table S2 (Supporting Information). The CoP@C system developed herein demonstrates comparable specific discharge capacity at 1.0 C with a low-capacity decay rate, showcasing the superiority of CoP@C as an efficient host material for Li–S batteries. The exceptional electrochemical performance of the CoP@C/S electrode can be attributed to the synergistic effect of the unique host structure derived from SPB and finely controlled CoP active sites. Specifically, electrically conductive hollow carbon nanospheres offer ample space for sulfur loading and facilitate rapid electron transfer within the electrode. The ultra-small CoP nanoparticles embedded in the hollow carbon nanospheres provide sufficient interfaces to chemically anchor intermediate polysulfides, thereby enhancing polysulfide conversion kinetics and suppressing the shuttle effect. Furthermore, the inherently polar ultra-small CoP nanoparticles enhance the redox reaction kinetics and improve sulfur utilization efficiency. These advantages are illustrated in Figure 6e.

Conclusions

In summary, we have synthesized ultra-small CoP nanoparticles with uniform size (7.1 ± 3.1 nm) embedded within hollow carbon nanospheres using SPB as the template and stabilizing assisted by PDA coating. The prevention of Co nanoparticle aggregation via electrostatic interactions between negatively charged brush and positively charged Co^{2+} facilitated the formation of ultra-small CoP particles. This engineered hybrid nanostructure exhibited exceptional polysulfide adsorption and catalytic effects, thus effectively mitigating the LiPSs shuttle while demonstrating superior electrical conductivity. Leveraging this well-designed structure, Li–S batteries based on the CoP@C/S electrode delivered a high initial specific discharge capacity of 850.0 mAh g^{-1} at 1.0 C and maintained 612.0 mAh g^{-1} after 900 cycles, with a low-capacity decay rate of 0.03% per cycle. We foresee the potential extension of this methodology to various nanostructured metal compounds, offering promising electrode materials not only for Li–S batteries but also for diverse energy applications.

Acknowledgements

Ping Feng acknowledges financial support of CSC scholarship (No. 202006630007). Qingping Wu is grateful for financial support provided by the Sino German (CSC-DAAD) Postdoc Scholarship Program (57678375). Open Access funding enabled and organized by Projekt DEAL.

Conflict of Interests

The authors declare no conflict of interest.

Data Availability Statement

The data that support the findings of this study are available from the corresponding author upon reasonable request.

Keywords: Lithium–sulfur batteries · Spherical polyelectrolyte brushes · CoP · Sulfur host · Nanospheres

[1] a) C. Zhang, R. Du, J. J. Biendicho, M. Yi, K. Xiao, D. Yang, T. Zhang, X. Wang, J. Arbiol, J. Llorca, Y. Zhou, J. R. Morante, A. Cabot, *Adv. Energy Mater.* **2021**, *11*, 2100432; b) P. Wang, B. Xi, Z. Zhang, M. Huang, J. Feng, S. Xiong, *Angew. Chem. Int. Ed.* **2021**, *60*, 15563–15571; c) C. Zhao, G. L. Xu, Z. Yu, L. Zhang, I. Hwang, Y. X. Mo, Y. Ren, L. Cheng, C. J. Sun, Y. Ren, X. Zuo, J. T. Li, S. G. Sun, K. Amine, T. Zhao, *Nat. Nanotech.* **2021**, *16*, 166–173; d) L. Shi, S.-M. Bak, Z. Shadike, C. Wang, C. Niu, P. Northrup, H. Lee, A. Y. Baranovskiy, C. S. Anderson, J. Qin, S. Feng, X. Ren, D. Liu, X.-Q. Yang, F. Gao, D. Lu, J. Xiao, J. Liu, *Energy Environ. Sci.* **2020**, *13*, 3620–3632.

[2] a) Q. Liu, J. Zhang, S. A. He, R. Zou, C. Xu, Z. Cui, X. Huang, G. Guan, W. Zhang, K. Xu, J. Hu, *Small* **2018**, *14*, e1703816; b) Z. Cui, S. A. He, Q. Liu, R. Zou, *Dalton Trans.* **2020**, *49*, 6876–6883; c) H. Wang, S.-A. He, Z. Cui, C. Xu, J. Zhu, Q. Liu, G. He, W. Luo, R. Zou, *Chem. Eng. J.* **2021**, *420*, 129693

[3] a) H. Wang, Z. Cui, S.-A. He, J. Zhu, W. Luo, Q. Liu, R. Zou, *Nano-Micro Lett.* **2022**, *14*, 189; b) F. Liu, P. Feng, M. Yuan, G. Zhai, M. T. Innocent, H. Xiang, Q. Wu, Y. Lu, M. Zhu, *ACS Sustain. Chem. Eng.* **2023**, *11*, 16544–16553; c) S. Mei, A. Siebert, Y. Xu, T. Quan, R. Garcia-Diez, M. Bär, P. Härtel, T. Abendroth, S. Dörfler, S. Kaskel, Y. Lu, *Batteries Supercaps* **2022**, *5*, e202100398.
[4] a) Q. Wu, Z. Yao, X. Zhou, J. Xu, F. Cao, C. Li, *ACS Nano* **2020**, *14*, 3365–3377; b) D. Xie, Y. Xu, Y. Wang, X. Pan, E. Härk, Z. Kochovski, A. Eljarrat, J. Müller, C. T. Koch, J. Yuan, Y. Lu, *ACS Nano* **2022**, *16*, 10554–10565; c) S. Zhang, X. Ao, J. Huang, B. Wei, Y. Zhai, D. Zhai, W. Deng, C. Su, D. Wang, Y. Li, *Nano Lett.* **2021**, *21*, 9691–9698.
[5] a) Y. Chen, W. Zhang, D. Zhou, H. Tian, D. Su, C. Wang, D. Stockdale, F. Kang, B. Li, G. Wang, *ACS Nano* **2019**, *13*, 4731–4741; b) H. Ci, J. Cai, H. Ma, Z. Shi, G. Cui, M. Wang, J. Jin, N. Wei, C. Lu, W. Zhao, J. Sun, Z. Liu, *ACS Nano* **2020**, *14*, 11929–11938; c) D. Gueon, M. Y. Ju, J. H. Moon, *Proc. Natl. Acad. Sci. USA* **2020**, *117*, 12686–12692.
[6] Y. Zhang, Y. Wang, R. Luo, Y. Yang, Y. Lu, Y. Guo, X. Liu, S. Cao, J. K. Kim, Y. Luo, *Nanoscale Horiz.* **2020**, *5*, 530–540.
[7] Y. Guo, J. Li, R. Pitcheri, J. Zhu, P. Wen, Y. Qiu, *Chem. Eng. J.* **2019**, *355*, 390–398.
[8] a) Z. Cheng, Z. Xiao, H. Pan, S. Wang, R. Wang, *Adv. Energy Mater.* **2017**, *8*, 1702337; b) L. Zhang, Y. Liu, Z. Zhao, P. Jiang, T. Zhang, M. Li, S. Pan, T. Tang, T. Wu, P. Liu, Y. Hou, H. Lu, *ACS Nano* **2020**, *14*, 8495–8507; c) Z. Ye, Y. Jiang, L. Li, F. Wu, R. Chen, *Adv. Mater.* **2020**, *32*, 2002168; d) Q. Wu, Z. Shadike, J. Xu, F. Cao, C. Li, *Energy Storage Mater.* **2023**, *55*, 73–83.
[9] a) W. Hou, P. Feng, X. Guo, Z. Wang, Z. Bai, Y. Bai, G. Wang, K. Sun, *Adv. Mater.* **2022**, *34*, 2202222; b) W. Liu, C. Luo, S. Zhang, B. Zhang, J. Ma, X. Wang, W. Liu, Z. Li, Q.-H. Yang, W. Lv, *ACS Nano* **2021**, *15*, 7491–7499; c) Y. Xie, J. Cao, X. Wang, W. Li, L. Deng, S. Ma, H. Zhang, C. Guan, W. Huang, *Nano Lett.* **2021**, *21*, 8579–8586.
[10] J. Zhou, X. Liu, L. Zhu, J. Zhou, Y. Guan, L. Chen, S. Niu, J. Cai, D. Sun, Y. Zhu, J. Du, G. Wang, Y. Qian, *Joule* **2018**, *2*, 2681–2693.
[11] a) F. Zhou, Y. Mei, Q. Wu, H. Li, J. Xu, H. Chen, *Energy Storage Mater.* **2024**, *67*, 103315; b) Q. Wu, X. Zhou, J. Xu, F. Cao, C. Li, *J. Energy Chem.* **2019**, *38*, 94–113.
[12] a) T. Xiao, F. Yi, M. Yang, W. Liu, M. Li, M. Ren, X. Zhang, Z. Zhou, *J. Mater. Chem. A* **2021**, *9*, 16692–16698; b) T. Meng, Y.-N. Hao, L. Zheng, M. Cao, *Nanoscale* **2018**, *10*, 14613–14626.
[13] a) Y. Ding, Q. Cheng, J. Wu, T. Yan, Z. Shi, M. Wang, D. Yang, P. Wang, L. Zhang, J. Sun, *Adv. Mater.* **2022**, *34*, 2202256; b) R. Wang, R. Wu, X. Yan, D. Liu, P. Guo, W. Li, H. Pan, *Adv. Funct. Mater.* **2022**, *32*, 2200424; c) R. Wang, J. Yang, X. Chen, Y. Zhao, W. Zhao, G. Qian, S. Li, Y. Xiao, H. Chen, Y. Ye, G. Zhou, F. Pan, *Adv. Energy Mater.* **2020**, *10*, 1903550; d) Y. Zhang, J. Liu, J. Wang, Y. Zhao, D. Luo, A. Yu, X. Wang, Z. Chen, *Angew. Chem. Int. Ed.* **2021**, *60*, 26622–26629; e) G. Zhou, S. Zhao, T. Wang, S.-Z. Yang, B. Johannessen, H. Chen, C. Liu, Y. Ye, Y. Wu, Y. Peng, C. Liu, S. P. Jiang, Q. Zhang, Y. Cui, *Nano Lett.* **2019**, *20*, 1252–1261.
[14] a) Q. Cheng, Z. Yin, S. Pan, G. Zhang, Z. Pan, X. Yu, Y. Fang, H. Rao, X. Zhong, *ACS Appl. Mater. Interfaces* **2020**, *12*, 43844–43853; b) J. Jin, W. Cai, J. Cai, Y. Shao, Y. Song, Z. Xia, Q. Zhang, J. Sun, *J. Mater. Chem. A* **2020**, *8*, 3027–3034.
[15] a) T. Quan, Y. Xu, M. Tovar, N. Goubard-Bretesché, Z. Li, Z. Kochovski, H. Kirmse, K. Skrodczky, S. Mei, H. Yu, D. Abou-Ras, M. Wagemaker, Y. Lu, *Batteries & Supercaps* **2020**, *3*, 747–756; b) Y. Lu, M. Ballauff, *Prog. Polym. Sci.* **2016**, *59*, 86–104.
[16] K. Guo, B. Xi, R. Wei, H. Li, J. Feng, S. Xiong, *Adv. Energy Mater.* **2020**, *10*, 1902913.
[17] L. Feng, R. Ding, Y. Chen, J. Wang, L. Xu, *J. Power Sources* **2020**, *452*, 227837.
[18] P. Feng, Z. Cui, S.-A. He, Q. Liu, J. Zhu, C. Xu, R. Zou, J. Hu, *J. Mater. Chem. A* **2019**, *7*, 24292–24300.
[19] P. Xue, K. Zhu, W. Gong, J. Pu, X. Li, C. Guo, L. Wu, R. Wang, H. Li, J. Sun, G. Hong, Q. Zhang, Y. Yao, *Adv. Energy Mater.* **2022**, *12*, 2200308.
[20] L. Liu, Y. Li, Y. Zhang, Z. Qiao, L. Lin, X. Yan, Z. Meng, Y. Huang, J. Lin, L. Wang, B. Sa, Q. Xie, D.-L. Peng, *Electrochim. Acta* **2022**, *419*, 140391.
[21] F. Y. Fan, W. C. Carter, Y. M. Chiang, *Adv. Mater.* **2015**, *27*, 5203–5209.
[22] a) M. Du, P. Geng, C. Pei, X. Jiang, Y. Shan, W. Hu, L. Ni, H. Pang, *Angew. Chem. Int. Ed.* **2022**, *61*, e202209350; b) Z. Jin, T. Lin, H. Jia, B. Liu, Q. Zhang, L. Li, L. Zhang, Z.-M. Su, C. Wang, *ACS Nano* **2021**, *15*, 7318–7327.
[23] D. S. Bin, Z. X. Chi, Y. Li, K. Zhang, X. Yang, Y. G. Sun, J. Y. Piao, A. M. Cao, L. J. Wan, *J. Am. Chem. Soc.* **2017**, *139*, 13492–13498.
[24] L. Liu, Y. Li, Y. Zhang, Z. Qiao, L. Lin, X. Yan, Z. Meng, Y. Huang, J. Lin, L. Wang, B. Sa, Q. Xie, D.-L. Peng, *Electrochim. Acta.* **2022**, *419*, 140391.
[25] S. Yao, C. Zhang, F. Xie, S. Xue, K. Gao, R. Guo, X. Shen, T. Li, S. Qin, *ACS Sustain. Chem. Eng.* **2020**, *8*, 2707–2715.

Manuscript received: April 4, 2024
Accepted manuscript online: June 5, 2024
Version of record online: August 2, 2024